New Zealand Journal of Geology and Geophysics

RESEARCH ARTICLE OPEN ACCESS

Holocene Slip Behavior and Shallow Structure of the Milun Fault at the Collision–Subduction Transition, Eastern Taiwan

Wen-Jeng Huang[1,2] | Ya-Chu Tseng[3] | Wen-Shan Chen[4] | I-Chin Yen[1] | Shao-Yi Huang[5] | Jiun-Yee Yen[6] | Shih-Ting Lu[7]

[1]Graduate Institute of Applied Geology, National Central University, Taoyuan, Taiwan | [2]Department of Earth Sciences, National Central University, Taoyuan, Taiwan | [3]Department of Earth Sciences, National Taiwan Normal University, Taipei, Taiwan | [4]Department of Geosciences, National Taiwan University, Taipei, Taiwan | [5]Science and Technology Research Institute for DE-Carbonization, National Taiwan University, Taipei, Taiwan | [6]Department of Natural Resorces and Environmental studies, National Dong Hwa University, Hualien, Taiwan | [7]Geological Survey and Mining Management Agency, Ministry of Economic Affairs, New Taipei city, Taiwan

Correspondence: Wen-Jeng Huang (huang22@ncu.edu.tw)

Received: 2 March 2026 | **Revised:** 3 May 2026 | **Accepted:** 8 May 2026

Keywords: earthquake recurrence | Milun Fault | oblique convergence | paleoseismology | slip partitioning | transpression | trenching

ABSTRACT

The Milun Fault forms the northernmost onshore segment of the Longitudinal Valley fault system, a plate-boundary suture between the Eurasian and Philippine Sea plates in eastern Taiwan, and poses a significant seismic hazard to Hualien City. Despite destructive earthquakes in 1951 and 2018, the shallow structure, long-term slip behavior, and paleoseismic history of the fault have remained poorly constrained due to limited direct exposure of its principal fault. New paleoseismic trench and borehole data provide direct constraints on the near-surface geometry of the principal fault and its associated branch faults. Trench exposures document a steeply east-dipping principal fault (~80°) accompanied by several branch faults, defining a zone of distributed deformation. Stratigraphic restoration, growth strata, colluvial wedges, and liquefaction features indicate five late Holocene surface-rupturing earthquakes, including the 1951 and 2018 events and three prehistoric earthquakes dated to 783–352, 2361–1302, and 3185–2303 cal yr BP. Borehole correlations indicate ~18.6 m of vertical separation since ~5.7 ka, corresponding to a long-term vertical slip rate of ~3.2–3.6 mm/yr. Stratigraphic relationships further indicate that the Milun Tableland emerged above sea level at ≈3.2 ka, implying cumulative uplift through repeated seismic events. Inter-event times range from decades to more than a millennium, and overlapping age constraints preclude definition of a characteristic recurrence interval. These results show that deformation along the Milun Fault is accommodated by a steep principal fault together with multiple branch faults, and that earthquake recurrence in this transpressional plate-boundary setting is temporally irregular.

1 | Introduction

Oblique convergence at collision–subduction transition zones commonly generates structurally complex fault systems in which deformation is partitioned among multiple structures and earthquake recurrence may be temporally irregular. In such settings, near-surface fault architecture influences the expression of surface rupture and the preservation of paleoseismic records. However, direct trench-scale constraints on how near-surface deformation affects the recording and interpretation of past earthquakes remain limited in many active plate-boundary systems.

Taiwan occupies the active boundary between the Philippine Sea Plate and the Eurasian Plate, where oblique convergence

proceeds at ~82 mm/yr (Yu et al. 1997) (Figure 1). The northernmost segment of the Longitudinal Valley Fault system represents a transition from arc–continent collision to subduction, forming a structurally complex plate-boundary zone in eastern Taiwan. Within this setting, the Milun Fault marks the northernmost onshore segment and accommodates active transpressional deformation. This deformation is expressed not only along the principal fault trace but also in the uplift of the adjacent Milun Tableland, a low-relief geomorphic surface located immediately north of Hualien City. The tableland forms a distinct topographic high relative to the surrounding alluvial plains, bounded to the west by the Milun Fault and to the east by the coastal margin (Figure 2). It is primarily composed of uplifted marine and marginal deposits, and its present morphology reflects late Quaternary uplift associated with ongoing transpressional deformation along the Milun Fault.

The Milun Fault is notable not only for its tectonic position but also for its recent seismic history. It is the only active fault in Taiwan directly associated with two destructive historical earthquakes: the 21 October 1951 Mw 7.0 Hualien earthquake sequence, which caused 68 fatalities and 856 injuries (Wang 2024), and the 6 February 2018 Mw 6.4 Hualien earthquake, which resulted in 17 deaths and 285 injuries (Wu et al. 2019). Because the fault runs directly beneath Hualien City—the most densely populated urban area (~100,000 residents) in eastern Taiwan—its behavior has important societal implications.

Previous investigations have documented coseismic surface ruptures (Huang et al. 2019; Hsu et al. 2019), geodetic deformation (Kuo et al. 2019; Tung et al. 2019; Wu et al. 2019), and short-term slip characteristics during the 2018 event (Yen et al. 2019; Lee et al. 2019). These studies constrain contemporary deformation but provide limited insight into the longer-term earthquake history and cumulative slip behavior of the fault. In particular, the shallow geometry of the principal fault and its relation to subsidiary structures remain poorly resolved, hindering evaluation of how slip is partitioned within the fault zone over millennial timescales.

In this study, we integrate new paleoseismic trench exposures with borehole correlations and stratigraphic analysis to reconstruct the late Holocene slip history of the Milun Fault. By directly constraining near-surface fault architecture and cumulative displacement, we evaluate the temporal pattern of earthquake recurrence and its structural controls within a transpressional plate-boundary setting. The Milun Fault thus provides a trench-scale example of how near-surface deformation, including fault branching and distributed strain, influences the expression of surface rupture and the preservation of paleoseismic records in obliquely convergent margins.

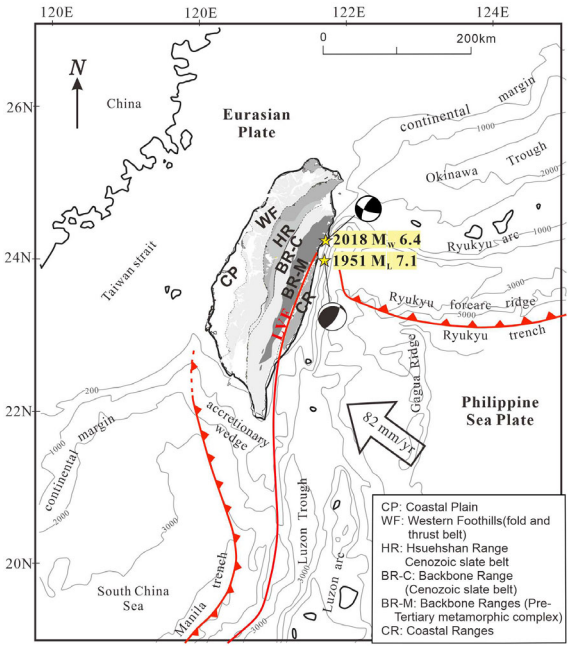

FIGURE 1 | Tectonic framework of Taiwan. Oblique convergence proceeds at ~82 mm/yr (Yu et al. 1997). Epicenters of the two historical earthquakes that produced surface ruptures in Hualien are indicated by stars, along with their focal mechanisms (Cheng et al. 1997 and Lee et al. 2019).

2 | Geology of Milun Fault

The 1951 Hualien earthquake sequence generated a surface-rupture trace in the Milun Fault, extending from Chihsingtan to Nanbin (Yang 1953; also see in Figure 3), representing the earliest geological evidence of activity associated with this fault. The fault is marked by a prominent scarp separating the northernmost Longitudinal Valley plain from the Milun Tableland. This northeast-trending scarp is ~4.4 km long, with a vertical relief of about 20 m in its northern segment that gradually decreases to ~5 m toward the south (Shih et al. 1983). Bathymetric data offshore Hualien suggest that this lineated scarp continues eastward beneath the sea, where it appears to connect with the toe of the Hualien Ridge (Figure 2). The uplift of the Milun Tableland has also caused a significant change in the course of the Meilun River. The river originates from streams draining the Central Range and flows eastward, but is abruptly deflected southward in front of the scarp before eventually reaching the Pacific Ocean at the southern end of the tableland. In addition, multiple levels of marine terraces preserved on the Milun Tableland are interpreted as evidence of repeated uplift events associated with past earthquakes (Shih et al. 1983; Yang et al. 1986).

The oldest exposed unit on the Milun Tableland is the Milunpi Conglomerate (Lin 1969; Lin et al. 2009), referred to as the Milun Conglomerate in the early times (Hsu 1956; Hsieh and Teng 1994). This unit crops out only along the eastern and northern cliffs of the tableland (Figure 3) and consists primarily of gravels derived from metamorphic rocks of the Central/Backbone Range (Figure 1). Neither its underlying nor overlying units are exposed. Its exposed thickness has been estimated to be ≈350 m (Hsu 1956) or about 300 m (Hsieh and Teng 1994). Based on the occurrence of the calcareous nannofossil *Gephyrocapsa oceanica* and the absence of *Pseudoemiliania lacunosa*, the unit is assigned to the Middle Pleistocene (Chi et al. 1983). Bedding planes of the Milunpi Conglomerate generally dip southward at ~30° (Hsu 1956). The upper part of the tableland is unconformably overlain by Holocene beach gravel deposits and coral reefs (Konishi et al. 1968;

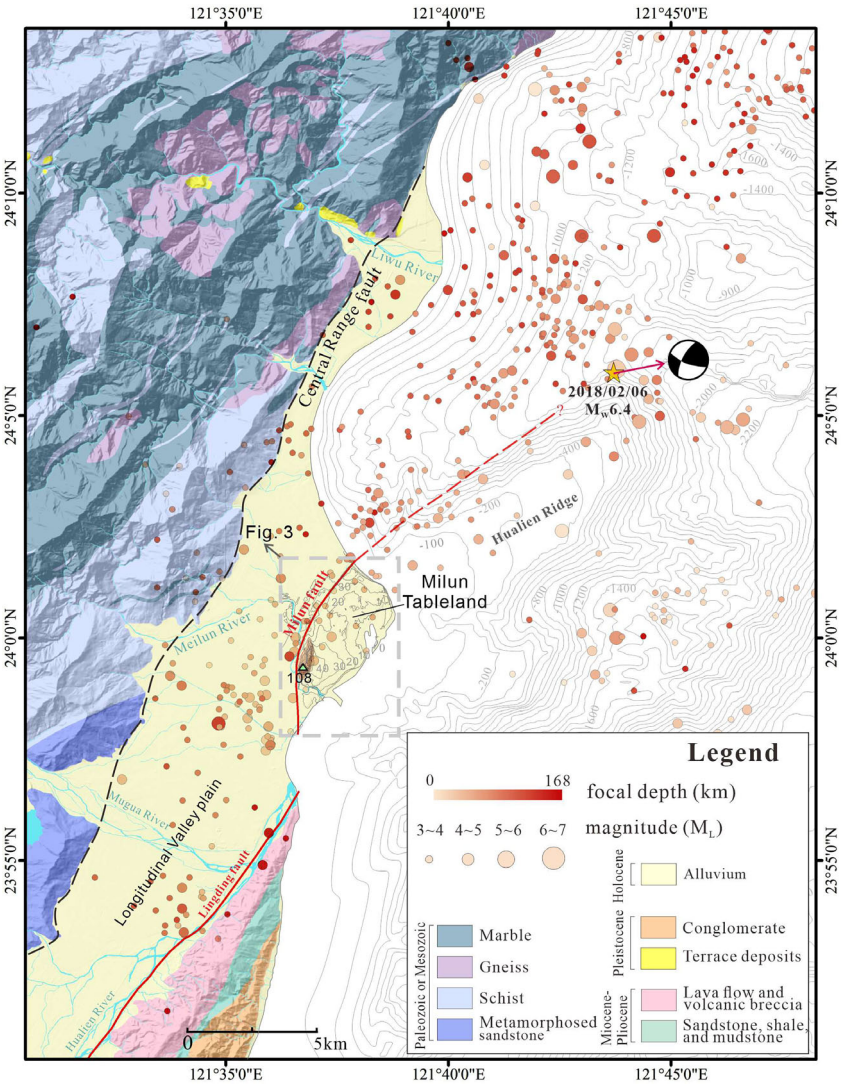

FIGURE 2 | Geologic map of the northernmost Longitudinal Valley with offshore bathymetry, and seismic sequence of the February 6, 2018 Hualien earthquake.

Lin 1969) known as Milun Formation (Figure 3). Stratigraphic facies analysis suggests that the Milunpi Conglomerate was deposited as a fan-delta in a shallow-marine environment (Hsieh and Teng 1994).

The main trace of the Milun Fault is defined at the contact where the Milunpi Conglomerate is thrust over unconsolidated deposits, as inferred from limited exposures along the northern coastline of the tableland. This contact, however, is largely obscured along the coast by dense vegetation and artificial structures. At the ground surface and within the upper few decimeters, the fault is expressed by fractures and minor thrust faults developed within these unconsolidated deposits (Huang et al. 2019). To date, no direct observations of the Milun Fault have been reported beneath these shallow surface deposits in natural exposures. Its polarity (i.e., dipping direction) to the east is generally accepted down to a few kilometers, but becomes debated at greater depths. Three possible geometries have been proposed (1) a consistently east-dipping fault (e.g., Chemenda et al. 2001), (2) a west-dipping fault (e.g., Rau et al. 2007), and (3) an east-dipping fault at shallow depth that transitions to a west-dipping geometry at greater depth (e.g., Yen et al. 2019). Recent borehole and seismic reflection observations provide new constraints on the steep, east-dipping geometry of the Milun Fault at depth, although the continuity of this geometry toward the near surface remains to be resolved.

Extensive urbanization across the Milun Tableland has limited natural exposures, leaving the shallow geometry and long-term deformation history of the Milun Fault poorly constrained, despite its recognition as a major active structure with an estimated length of ~8 km (e.g., Lin et al. 2009). In particular, the main fault trace has never been directly exposed near the surface. To address these uncertainties, this study aims to (1) constrain the near-surface geometry and sedimentary deformation associated with the Milun Fault through trench excavations, and (2) quantify its long-term slip behavior using borehole core data integrated with stratigraphic and chronological analyses.

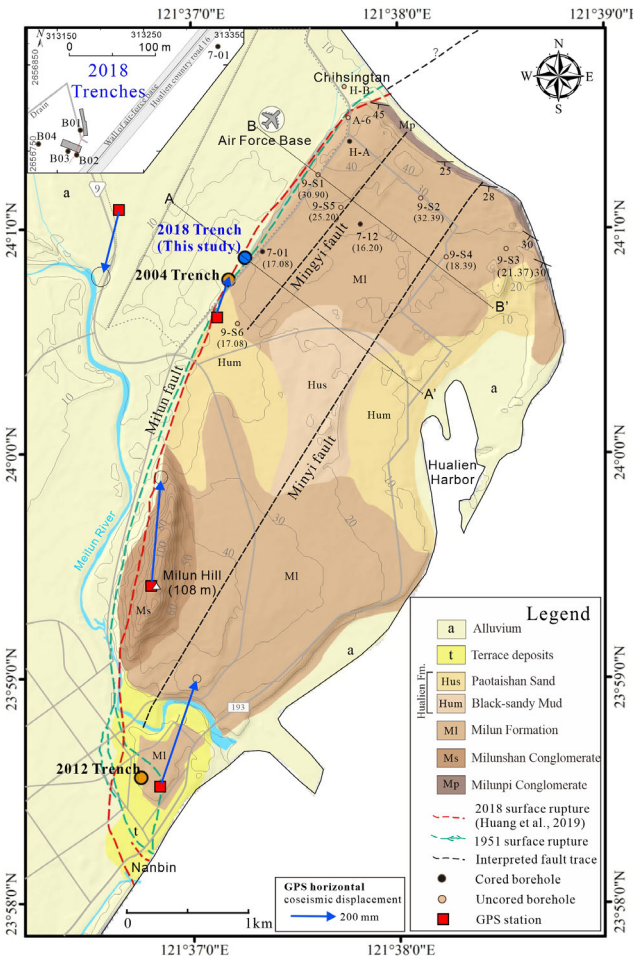

FIGURE 3 | Geological map of the Milun Tableland showing GPS horizontal displacements, modified after Tung et al. (2019). The displacement vectors indicate a left-lateral sense of shear across the Milun Fault. The number in parentheses following each borehole denotes the elevation of the top of the Milunpi Conglomerate. Black dashed lines represent interpreted or concealed fault traces, including the Mingi Fault proposed by Yamaguchi and Ota (2002) and the Minyi Fault suggested by Lin and Hsiao (1998). Except for the MiDAS boreholes H-B and H-A (Ma et al. 2024), all borehole data were obtained from the Engineering Geological Investigation Databank maintained by the Geological Survey and Mining Management Agency, Ministry of Economic Affairs (MOEA), Taiwan.

3 | Previous Paleoseismic Studies of the Milun Fault

3.1 | 2004 and 2012 Trenching

Prior to this study, paleoseismic investigations of the Milun Fault were conducted at two sites excavated in 2004 and 2012 (Chen 2004; Chen et al. 2012; Figure 3). Although these studies documented deformation within shallow sedimentary deposits along the western margin of the Milun Tableland, neither excavation directly exposed the principal fault trace.

The 2004 trench, located near the eastern wall of the Hualien Air Force Base, revealed tilting and flexural deformation within shallow marine and colluvial deposits at the base of the topographic scarp. Differences in bedding attitude between trench exposures and nearby outcrops were interpreted to reflect folding associated with fault activity. However, the principal fault surface itself was not intersected, and displacement estimates were therefore indirect.

The 2012 investigation, situated ≈1 km south of Milun Hill, comprised two trenches and multiple boreholes. These exposures documented angular unconformities, localized flexure, and minor offsets within late Holocene sediments. Radiocarbon ages from organic-rich and marine deposits constrained deformation to the late Holocene and were used to infer a minimum uplift rate of >2.45 mm/yr. Nevertheless, deformation was expressed primarily as folding and minor faulting within shallow strata, and the main fault strand was again not directly exposed.

Collectively, the 2004 and 2012 excavations demonstrated ongoing late Holocene deformation along the western margin of the Milun Tableland but left several key questions unresolved. In particular, the near-surface geometry of the principal Milun Fault, the partitioning of displacement within the Milun Fault zone, and the direct stratigraphic expression of surface-rupturing earthquakes remained uncertain. These limitations motivated the new trenching undertaken in this study, which was positioned closer to the projected fault trace in order to directly constrain the shallow architecture and paleoseismic history of the Milun Fault.

3.2 | Long-Term Uplift Rate of the Milun Tableland

All available estimates of the long-term uplift rate of the Milun Tableland are summarized in Table 1. Bonilla (1975) proposed an uplift rate of 4.6–8.7 mm/yr based on radiocarbon dating of elevated marine deposits. Yamaguchi and Ota (2002) estimated an uplift rate of 4.5–5.1 mm/yr for the northern portion of the Milun Tableland using radiocarbon dating of corals on Holocene marine terraces, and further noted that the height of the Milun Fault scarp decreases southward. As noted in the previous section, Chen et al. (2012) inferred an uplift rate greater than 2.45 mm/yr over the past ~1900 years from deformation features and dating results in an excavated trench. Chen (2013) estimated uplift rates of 6.91–6.93 mm/yr for marine terraces on the Milun Tableland using U–Th radiometric dating. Collectively, these studies indicate a range of long-term Holocene uplift rates for the Milun Tableland, reflecting the cumulative influence of all probable structures within the area.

4 | Present Study

A surface rupture associated with the 2018 Hualien earthquake was observed along the toe of the western edge of the Milun Tableland, within the Air Force Base, several hundred meters north of the 2004 trench site (Figure 4). At this location, the rupture consisted of a series of right-stepping en echelon opening fractures, suggesting formation under left-lateral shear. Two trenches were excavated across the rupture. A 2 m-wide drainage channel lay between them, trending SSE across the plain and bending to ESE at the slope toe. The trench northeast of the channel, designated Trench 1, was excavated first. It was opened in

TABLE 1 | Uplift rate of the Milun Tableland.

Reference	Sample ID (Original source)	Elevation (m a.s.l.)	14C age	U-Th age (yr BP)	Uplift rate (mm/yr)
Bonilla (1975)	CT-1 (Konishi et al. 1968)	25	2880 ± 120 (yr BP)	—	8.7
	NTU-5 (Lin 1969)	20	3990 ± 269 (yr BP)	—	5.2
	NTU-13 (Lin 1969)	14	3200 ± 300 (yr BP)	—	4.6
Yamaguchi and Ota (2002)	HT28	12	2618–2297 (cal. yr BP)	—	4.5–5.1
Chen et al. (2012)	HKS2-005	5	1820–1630 (cal. yr BP)	—	2.45
Chen (2013)	ML-004	27.29	—	3936 ± 16	6.91–6.93

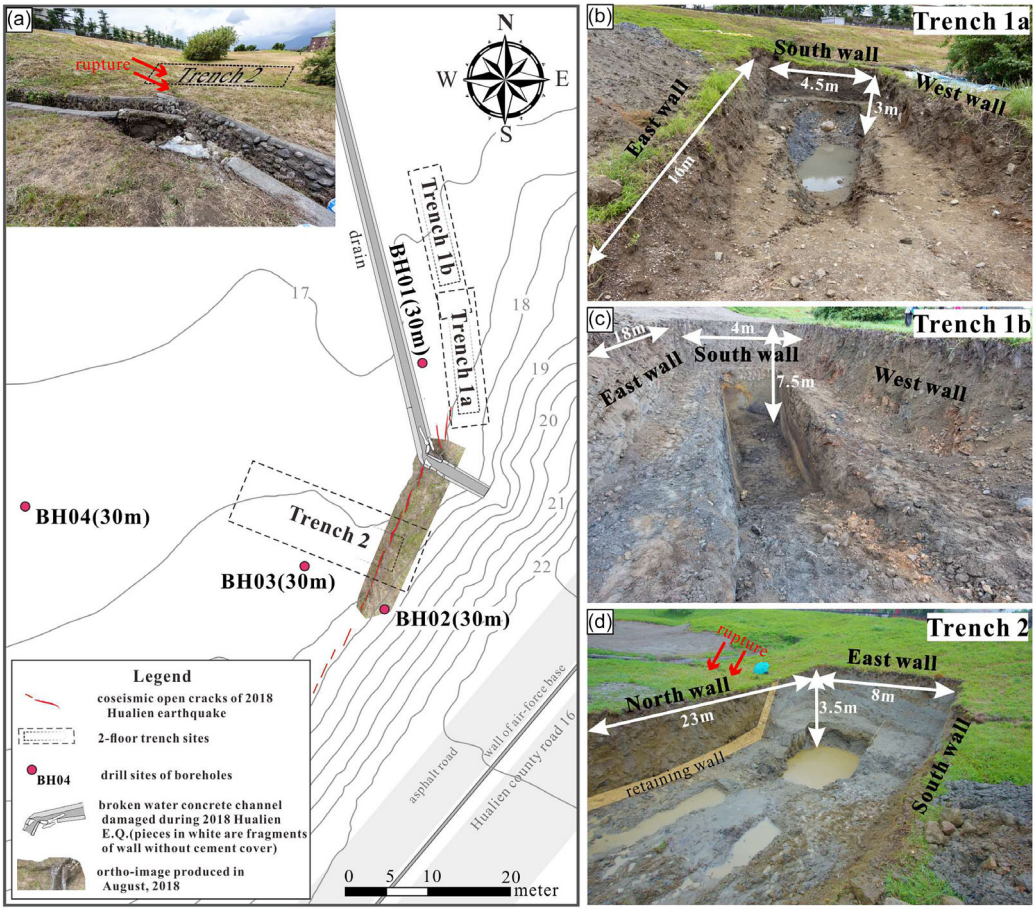

FIGURE 4 | (a) Setting of 2018 Trenches along with the 2018 coseismic surface rupture and boreholes BH01–BH04 at Hualien Air Force Base. (b) Trenche 1a; (c) Trench 1b; (d) Trench 2. Red dashed lines denote open cracks produced by the 2018 Hualien earthquake. Trench photographs illustrate excavation geometry and scale; Trench 1b partly overlaps the southern end of Trench 1a, and Trench 2 was excavated across the rupture zone south of Trench 1.

two stages: Trench 1a, followed by Trench 1b after Trench 1a had been backfilled, with an overlap of ≈3 m. This trench was positioned adjacent to and subparallel with the SSE-trending portion of the channel. The second excavation, Trench 2, was oriented ESE and located more than 8 m southwest of the channel. In addition, four boreholes were drilled to depths of 30 m: three aligned with Trench 2 and one positioned between Trench 1 and the channel.

4.1 | Trenches

Trench 1 had a combined length of 31 m, whereas Trench 2 measured 23 m. Both trenches were excavated in two stages, with Trench 1 including an additional deeper cut (Trench 1b) beneath the initial excavation. Immediately after excavation, the exposures were documented with dimensions (length, width, and depth in meters) shown in Figure 4. All trench walls were

photographed, and these photographs were later processed into orthorectified images (Figures 5b and 6b) using Pix4D software.

Groundwater at the site was shallow. Excavation reached a gravelly aquifer at depths of 3–3.5 m at the eastern ends of the trenches. Groundwater flowed through this gravelly layer and gradually filled the lower parts of the trenches up to the elevation of the gravelly horizon.

The previously mentioned en echelon fractures extended across the site of Trench 2 and terminated at the western edge of Trench 1. Excavation revealed that the fractures at Trench 2 were located directly above an underground L-shaped concrete retaining wall. This wall extended to a depth of about 2 m and was overlain by backfill. Due to the high groundwater level and the presence of backfill, useful information was only obtained from the eastern end of the Trench 2 and has been integrated into the stratigraphic column of borehole BH-01 (Figure 6). Details are provided in the supplementary materials. Therefore, the following descriptions and discussions focus exclusively on Trench 1.

4.1.1 | Classification of Sedimentary Layers in Trench 1

The sedimentary sequence in Trench 1 is divided into nine stratigraphic units in addition to the backfill, numbered sequentially from Unit 1 (youngest) to Unit 9 (oldest). The deepest deposit, Unit 9, consists of a semilithified, matrix-supported conglomerate with a clay-sized matrix. It is poorly sorted, with gravel diameters ranging from 1 to 10 cm, and its total thickness remains unknown because the base was not exposed. Unit 9 is tentatively correlated with the Milunpi Conglomerate exposed along the Chihsingtan coast. Overlying Unit 9, Unit 8 is a gravel-supported sandy gravel with a yellowish sand matrix. Gravel sizes range from a few centimeters to several tens of centimeters, and sorting is similarly poor. The contact between Units 9 and 8 is an angular unconformity with a dip of ≈12°. Two quartzose boulders were found on the contact. Shortly after excavation, they slid down because of their weight (Figure 4b). Above Unit 8, Unit 7 is a gray, medium-grained sand layer. Units 9 through 7 are exposed only in the hanging wall of the principal fault, which complicates displacement estimates because marker horizons traceable across both the hanging wall and footwall are absent.

Unit 6 is dominated by medium-grained sand and can be subdivided into three subunits. Unit 6a consists of medium-grained sand with thin gravel interbeds, whereas Unit 6b is composed of interbedded coarse- and medium-grained sand. Unit 6c is mainly composed of medium-grained sand. Unit 6b conformably overlies Unit 6a. Both Units 6a and 6b are thrust over Unit 6c. Collectively, Units 9–6 record deposition in a marine environment. Sea shells and shell fragments were observed within these deposits.

Unit 5 is a black, muddy deposit enriched in carbonaceous material and is interpreted as a marsh deposit. Overlying this, Unit 4 is a large, wedge-shaped body of yellowish, medium-grained sand attributed to colluvial processes. Unit 3 is further subdivided into five subunits (3a–3e), consisting of medium sand, fine sand, and clay. These subdivisions are distinguished mainly by color differences; notably, Units 3a and 3c are darker brown and contain more organic material, suggesting that they were once exposed at the ground surface. Unit 2 is an orange-yellow, fine-grained sand layer that forms a wedge truncating the top of Unit 3. At its base, Unit 2 incorporates angular clasts derived from Unit 3, which are interpreted as reworked fragments produced during the deposition of the colluvial wedge. Finally, the uppermost

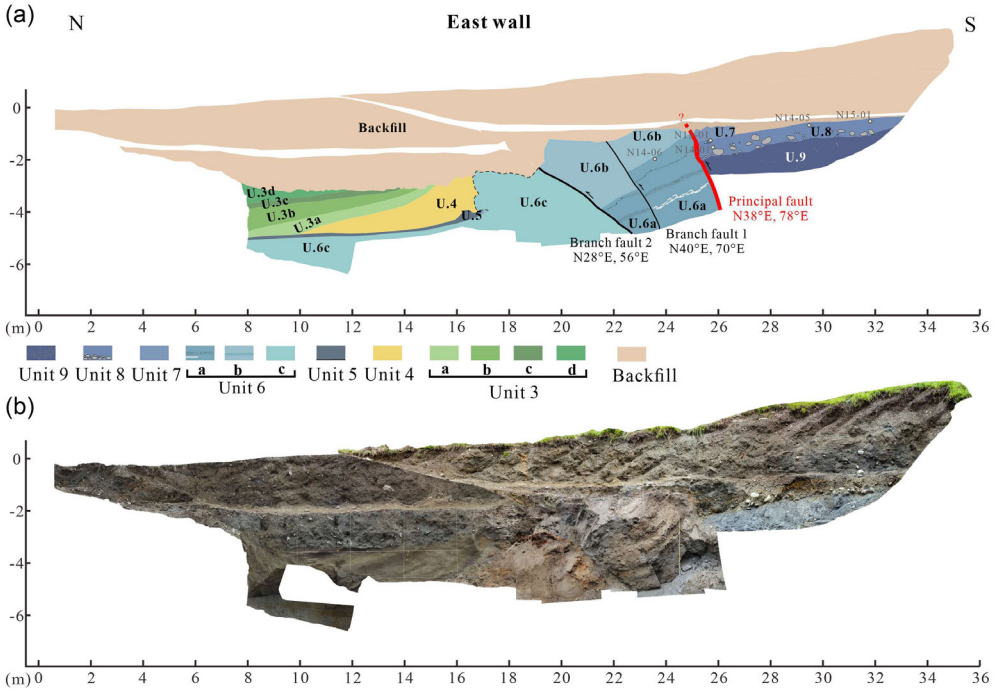

FIGURE 5 | East wall of the 2018 trench. (a) Interpreted log of the east wall showing stratigraphic units from Unit 9 (oldest) to Unit 3 (youngest). Faults and backfill are indicated, with unit subdivisions labeled. Locations of radiocarbon dating samples are marked in gray. (b) Orthophoto mosaic of the east wall corresponding to panel (a).

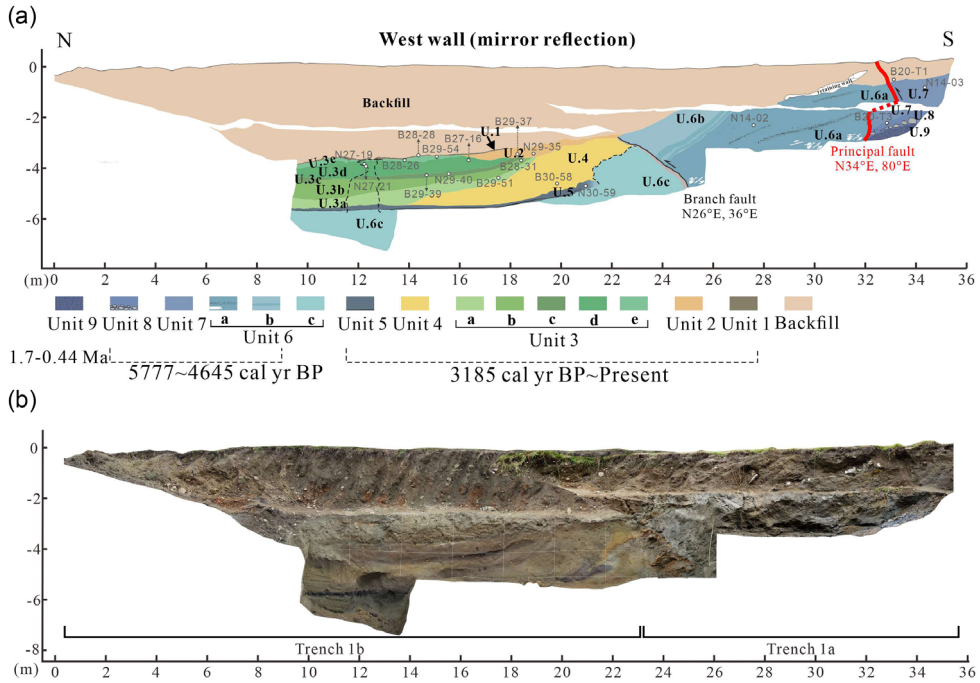

FIGURE 6 | West wall of the 2018 trench. (a) Interpreted log of the west wall showing stratigraphic units from Unit 9 (oldest) to Unit 1 (youngest). Faults and backfill are indicated, with unit subdivisions labeled (e.g., U.6a, U.6b). Locations of radiocarbon dating samples are marked in gray. (b) Orthophoto mosaic of the west wall corresponding to panel (a).

stratum directly beneath the backfill is Unit 1, a thin, dark, organic-rich horizon.

4.1.2 | Sub-Surface Structures in Trench 1

Both a principal fault and subsidiary branch faults were identified in Trench 1 (Figures 5 and 6). The principal fault is defined by the exposure of Unit 9, and its fault plane can be traced upward to the surface rupture produced by the 2018 Hualien earthquake on the west wall of the trench. Rather than a single plane, the principal fault zone consists of several shear planes, striking N34°E and dipping 80° eastward in the subsurface (Figure 6).

Branch faults were also observed within the trench. On the west wall, a single branch fault dips 36°, whereas on the east wall two branch faults dip 56° and 70°, respectively. This asymmetry may suggest that the single branch fault observed in the west wall bifurcates into two separate fault planes on the opposite wall. Because marker horizons suitable for measuring displacement are absent, it is not possible to estimate the offsets along the principal fault and one of its branch faults within this trench. Instead, displacement estimates for the Milun Fault will rely on borehole data.

At the footwall of the branch fault on the west wall, Unit 3 exhibits growth strata characterized by upward pinching and gently inclined bedding. These strata are folded near the branch fault, suggesting that the deformation is related to past seismic activity and slip along the Milun Fault. Evidence of liquefaction was also observed in parts of the trench, further supporting the occurrence of paleo-earthquakes. For example, Unit 6c intrudes into Units 5 and 4 in the central portion of Trench 1, consistent with liquefaction-induced injection. Collectively, these indicators—including colluvial wedges, growth strata, and liquefaction—provide critical evidence for reconstructing the paleoseismic history recorded in Trench

4.2 | Boreholes

Correlatable marker horizons were not clearly traceable across the fault in Trench 1. Four boreholes were therefore drilled to better constrain subsurface geometry and cumulative displacement. Borehole BH-02 was positioned on the hanging wall of the principal fault, whereas BH-01, BH-03, and BH-04 were located on the footwall (Figure 4).

A distinctive black, muddy horizon correlated with Unit 5 in Trench 1 was encountered only in the footwall boreholes, providing an important stratigraphic reference level. Beneath this horizon, all boreholes penetrated marine strata that can be correlated with Units 6–8 exposed in the trench.

At depth, a laterally continuous gravel layer provides a key marker for displacement analysis. This unit is present at the base of the footwall boreholes and occurs at shallower depth (4.1–5.0 m) in BH-02 on the hanging wall. Correlation of the upper boundary of this gravel horizon indicates a vertical separation of ≈17.9–18.6 m across the fault zone.

The horizontal distance measured normal to the fault between BH-02 and BH-01 is ≈7 m (Figure 7). Using this geometry, the minimum dip of the principal fault is estimated to be ∼69°, consistent with the steep orientation observed in Trench 1.

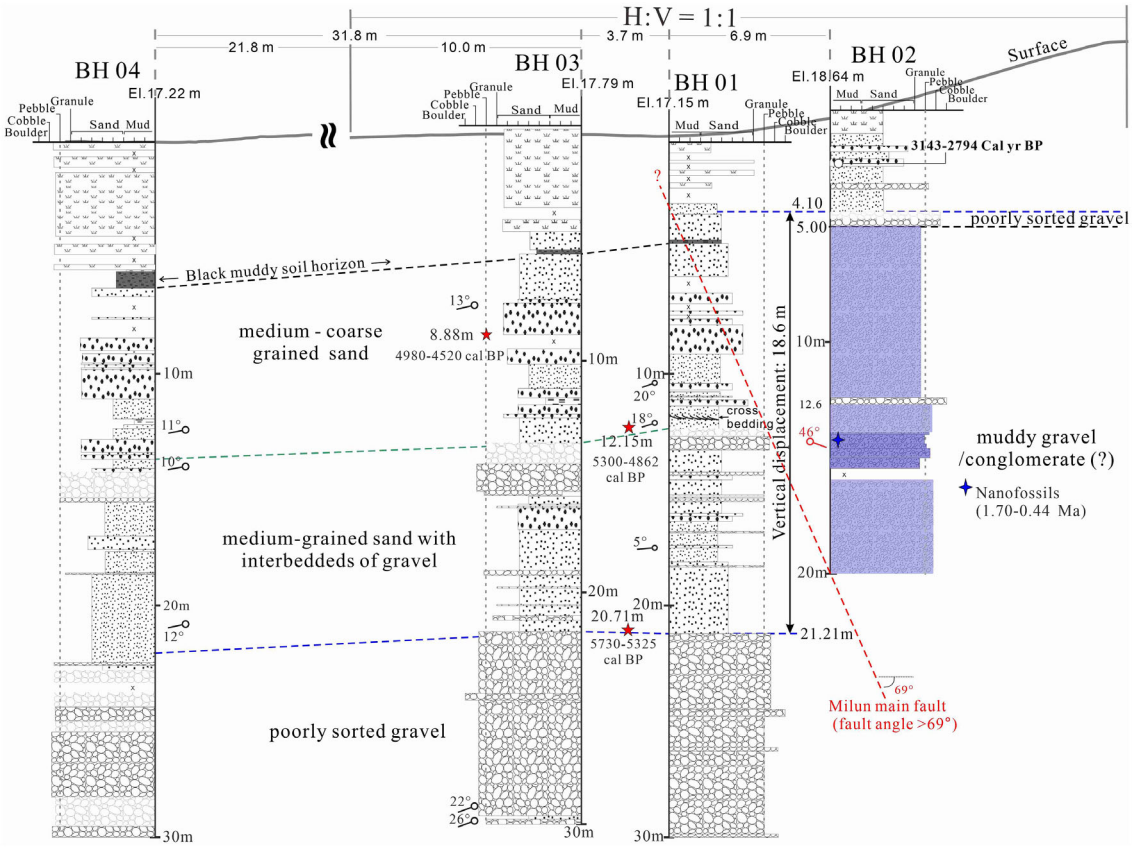

FIGURE 7 | Correlation of boreholes (BH01–BH04) across the Milun Fault. Stratigraphic columns are projected at a 1:1 horizontal-to-vertical scale (H:V = 1:1). Correlated horizons (dashed lines) constrain ≈18.6 m of vertical displacement across the steeply dipping main fault (dip > ~69°). Cross symbols indicate intervals where no core was recovered during drilling. Semitransparent intervals denote sections where most of the matrix was washed out during core retrieval.

Strata between the basal gravel (i.e., the poorly sorted gravel in Figure 7) and the overlying muddy soil horizon are consistently developed on both sides of the fault and can be subdivided into two stratigraphic packages recognizable in both the trench and boreholes. Their continuity supports the reliability of cross-fault correlation.

Unit 9, correlated with the Milunpi Conglomerate, was encountered exclusively in BH-02 on the hanging wall. A shear plane observed within this unit further confirms proximity to the principal fault. The absence of this unit in the footwall boreholes reinforces the interpretation that the fault lies between BH-02 and BH-01.

Borehole correlations therefore constrain both the steep near-surface geometry of the Milun Fault and a cumulative vertical displacement of ≈18.6 m since deposition of the correlated marker horizon.

4.3 | Radiocarbon (^{14}C) Dating Results

To determine the depositional ages of the units in Trench 1 and to evaluate the timing of paleo-earthquake events, radiocarbon dating was conducted on samples collected from Trench 1, Trench 2, and nearby boreholes. The samples were processed at BETA (Beta Analytic Testing Laboratory) and NTUAMS (National Taiwan University AMS Laboratory) using accelerator mass spectrometry. We report the calibrated age ranges at the 95.4% confidence level. A complete list of the dating results is provided in Table 2 and illustrated on the sedimentary column in Figure 8. The radiocarbon ages constrain the onset of terrestrial deposition (Units 5–1) to after ~3200 cal BP, based on the oldest age obtained from Unit 5 (3185–3000 cal BP). In contrast, Units 6–8, which contain marine deposits, yield ages ranging from ≈6200–5000 cal BP. These results indicate a transition from marine to terrestrial sedimentation at ≈3.2 ka, marking the emergence of the Milun Tableland in the study area.

5 | Discussion

5.1 | Holocene Long-Term Vertical Slip Rate

Prior to estimating the Holocene vertical slip rate, it is necessary to confirm that Unit 9 exposed in Trench 1 and BH-02 corresponds to the Milunpi Conglomerate. Correlation is supported by regional borehole data across the northern Milun Tableland (Figure 3) and by the presence of diagnostic nannofossils (*G. oceanica* and *P. lacunosa*) identified within BH-02, which constrain deposition to between 1.70 and 0.44 Ma. These constraints support assignment of Unit 9 to the Milunpi Conglomerate and indicate that the principal fault exposed in Trench 1 represents the main Milun Fault.

TABLE 2 | Radiocarbon dating results and sample information.

Trench (Sed. Horizon) & Borehole		Sample label	F	F error	Conventional age (BP)	Age error	Calibrated age (cal yr)	Material	Calibration method
Trench 1	Backfill	B20-T1-w	1.2827	0.0048	−2000	30	1979-1980 AD	Wood	INTCAL20+NHZ3
	Unit 1	B28-28-w	1.4294	0.0053	−2870	30	1973-1974 AD	Charcoal	INTCAL20+NHZ3
	Unit 2	B29-37-w	1.5384	0.0057	−3460	30	1969-1971 AD	Charred material	INTCAL20+NHZ3
		N29-35-w	0.9816	0.0065	149	53	155-0 BP	Charcoal	INTCAL20
	Unit 3e	B28-26-w	0.9852	0.0037	120	30	271-209 BP	Charcoal	INTCAL20
		B29-54-w	0.8153	0.0030	1640	30	1354-995 BP	Shell	MARINE20
	Unit 3d	B27-16-w	0.9730	0.0036	220	30	310-264 BP	Charcoal	INTCAL20
		N27-19-w	1.2989	0.0093	−2101	58	1978-1980 AD	Charcoal	INTCAL20+NHZ3
		N27-21-w	0.9708	0.0059	238	49	447-352 BP	Charcoal	INTCAL20
	Unit 3c	B29-39-w	0.9018	0.0034	830	30	783-683 BP	Charred material	INTCAL20
		N29-40-w	0.9178	0.0061	689	53	719-708 BP	Charcoal	INTCAL20
	Unit 3b	B28-31-w	0.8338	0.0031	1460	30	1384-1302 BP	Organic sediment	INTCAL20
	Unit 3a	B29-51-w	1.0802	0.0040	−620	30	2001-2003 AD	Plant material	INTCAL20+NHZ3
		N28-30-e	1.2423	0.0075	−1743	48	1981-1983 AD	Charcoal	INTCAL20+NHZ3
	Unit 4	B30-58-w	0.7501	0.0028	2310	30	2361-2303 BP	Organic sediment	INTCAL20
	Unit 5	N30-59-w	0.6436	0.0118	3540	147	4185-3457 BP	Soil material	INTCAL20
		B27-18-s	0.6798	0.0025	3100	30	3382-3227 BP	Organic sediment	INTCAL20
		B27-24-s	0.6926	0.0026	2951	30	3185-3000 BP	Organic sediment	INTCAL20
	Unit 6a	N14-02-w	0.5596	0.0031	4663	45	5184-4645 BP	Shell	MARINE20
		N14-06-e	0.5096	0.0057	5415	90	6026-5479 BP	Shell	MARINE20
	Unit 7	N14-03-w	0.5391	0.0029	4963	43	5494-5011 BP	Shell	MARINE20
	Unit 8	B20-T3-w	0.4900	0.0018	5730	30	6284-5909 BP	Shell	MARINE20
		N15-01-e	0.5233	0.0027	5202	41	5730-5315 BP	Shell	MARINE20
		N14-05-e	0.5291	0.0049	5114	74	5697-5188 BP	Shell	MARINE20
		N14-01-e	0.5234	0.0039	5201	60	5753-5298 BP	Shell	MARINE20
		N13-01-e	0.5212	0.0030	5234	46	5777-5327 BP	Shell	MARINE20
Borehole 01		BH01-2	0.5228	0.0020	5210	31	5730-5325 BP	Shell	MARINE20
Borehole 01		BH01-4	0.5488	0.0020	4820	29	5300-4862 BP	Shell	MARINE20

(Continues)

TABLE 2 | (Continued)

Trench (Sed. Horizon) & Borehole	Sample label	F	F error	Conventional age (BP)	Age error	Calibrated age (cal yr)	Material	Calibration method
Borehole 03	BH03	0.5668	0.0021	4561	30	4980-4520 BP	Shell	MARINE20
Trench 2	B29-32-s	0.0993	0.0009	18553	73	22681-22298 BP	Organic sediment	INTCAL20
	B27-08-s	0.7022	0.0052	2840	59	3149-3118 BP	Organic sediment	INTCAL20

Note: 1. delta R of −155 ± 59 from Penghu islands (Wang et al. 2025); 2. Calibration curve for terrestrial sample: INTCAL20; Calibrated curve for marine sample: MARINE 20 (Stuiver and Reimer 1993; Heaton et al. 2020; Reimer et al. 2020); 3. Post 1950 AD sample is calibrated by NHZ3 (Reimer, Brown and Reimer 2004; Reimer and Reimer 2026)

Unit 9 is encountered exclusively in BH-02 on the hanging wall, indicating that the principal fault lies between BH-02 and BH-01. Although the boreholes did not directly intersect the fault plane (Figure 7), correlation of stratigraphic markers across the fault constrains its geometry and displacement. The minimum dip derived from borehole projection is ≈69°, consistent with the steep orientation observed in the trench.

Correlation of a laterally traceable gravel horizon across the hanging wall and footwall indicates a cumulative vertical separation of ∼18.6 m. A shell sample collected near the top of this correlated interval in BH-01 yielded an age of 5730–5325 cal BP, indicating deposition prior to ∼5.7 ka. Dividing the measured vertical separation by this age constraint yields a Holocene vertical slip rate of ∼3.2–3.5 mm/yr over the past ∼6 ka.

To ensure reliability, an independent stratigraphic marker was examined. The gray medium- to coarse-grained sandstone overlying the basal gravel shares lithologic and stratigraphic characteristics with Unit 7 in Trench 1, and both units yield consistent age constraints (Figures 3 and 7). The stratigraphic separation of this sandstone is ∼18.7 m, corresponding to a Holocene vertical slip rate of 3.2–3.6 mm/yr, consistent with the gravel-based estimate and reinforcing its reliability.

Previously reported uplift rates of 4.5–8.7 mm/yr, derived from raised marine deposits and coral terraces along the coastline (Bonilla 1975; Yamaguchi and Ota 2002; Chen 2013), are higher than our estimate. However, these values represent net surface uplift relative to sea level, whereas our estimate is based on vertical displacement across the principal fault; thus, the two measures are not directly comparable. Coastal uplift likely reflects a combination of processes, including tilting of the hanging wall and deformation distributed across a finite-width zone (Yen et al. 2019), rather than displacement localized solely at the fault trace.

In contrast, slip along the Milun main fault may be partitioned among multiple fault branches. The same cross-bedded strata are identified in both Trench 1 and borehole BH-01 (Figure 9), but exhibit a vertical offset of ∼7.2 m. This offset suggests that displacement may not be confined to a single discrete fault plane, but is accommodated across multiple structures within the fault zone. Without direct exposure of the principal fault trace in Trench 1, the Holocene vertical slip rate would have been underestimated at ∼1.36–1.48 mm/yr. The left-lateral component of slip remains difficult to quantify because trench orientation does not allow reliable measurement of horizontal displacement.

5.2 | Restoration of Trench Profiles and Identification of Paleo-Earthquake Events

Reliable restoration of geological profiles requires correlatable stratigraphic markers across the hanging wall and footwall. Although no ideal index layers are exposed in Trench 1, multiple indirect geological indicators—including growth strata, colluvial wedges, and liquefaction features—allow reconstruction of several paleo-earthquake events over the past few thousand years. Based on these lines of evidence, at least five events are inferred during the last ∼4 ka, including the 1951 and 2018 earthquakes

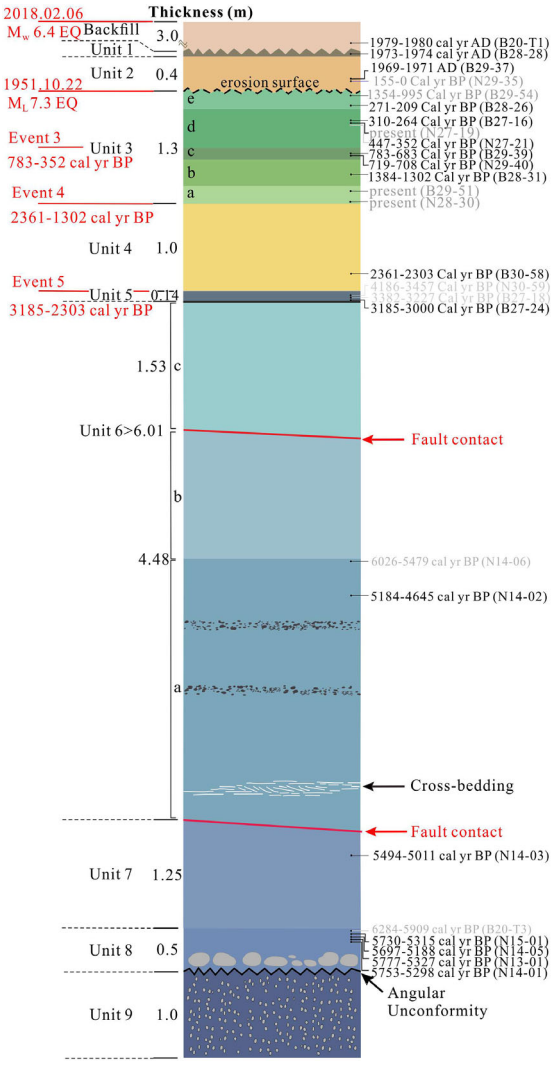

FIGURE 8 | Stratigraphic column of Trench 1 showing sedimentary units and fault contacts. Calibrated radiocarbon ages are indicated and used to constrain the timing of paleo-earthquake events.

(Table 3; Figure 10). The deformation history recorded in Trench 1 was therefore reconstructed through sequential restoration of the stratigraphic profiles, guided by observed structural and stratigraphic relationships.

5.2.1 | Event 1 (2018 Earthquake)

The most recent deformation (Event 1) corresponds to the 2018 Hualien earthquake (Figure 10a). The key evidence is that the main fault planes exposed on both trench walls align with the surface ruptures produced during the 2018 event. Because the fault tip terminated just below the ground surface, we infer that it reached the boundary between Unit 7 and the backfill deposits.

5.2.2 | Event 2 (1951 Earthquake)

The second event corresponds to the 1951 Hualien earthquake (Figure 10b). The primary evidence is the presence of Unit 2, a wedge-shaped deposit dated to A.D. 1969–1971 (Figure 8). Its geometry and position on the footwall side of the main fault indicate a colluvial wedge—a diagnostic product of surface faulting. For the restoration, Unit 2 was removed, since it truncates Unit 3.

5.2.3 | Event 3 (783–352 cal yr BP)

The third event is represented by folded growth strata deposited between ≈2000 and 352 cal yr BP (Figures 7 and 10c). On the west wall, growth strata (Units 3a–3c) display inclined bedding and thinning toward the fault, typical features of progressive folding above an active fault. Restoration involved unfolding these units until their boundaries became subhorizontal, yielding an estimated minimum fault throw of ~1.23 m. Units 3d and 3e, which do not show the same growth-strata characteristics, were excluded from the restoration. The event age is bracketed by the depositional ages of Units 3c and 3d.

5.2.4 | Event 4 (2361–1302 cal yr BP)

Event 4 is identified from evidence of liquefaction, a reliable indicator of seismic shaking (Figure 10d). Unit 6b, mainly composed of marine deposits, intrudes upward into Units 4 and 5, suggesting that liquefaction occurred during strong ground motion. Restoration of this feature indicates that Unit 4 originally formed a wedge-shaped colluvial deposit prior to liquefaction, yielding an estimated fault throw of ~0.98 m on the west wall and ~1.0 m on the east wall.

5.2.5 | Event 5 (3185–2303 cal yr BP)

The fifth and earliest event is represented by the colluvial wedge (Unit 4), which likely formed during an earthquake (Figure 10e). Its age is older than the deposition of Unit 4, dated at 3830–2184 cal yr BP. This represents the earliest seismic event recognized in Trench 1. Restoration of this feature yields an estimated fault throw of ~0.6 m on the west wall and ~0.51 m on the east wall.

In addition to these five identified events, a marked shift in depositional environment from marine (Unit 6) to terrestrial (Unit 5) indicates an important tectonic transition. This boundary suggests that the Milun Tableland began to emerge above sea level approximately three thousand and two hundred years ago, at least in its northern part. However, the exact number of paleo-earthquake events that collectively produced this uplift remains uncertain.

5.3 | Earthquake Recurrence Interval of the Milun Fault

Five paleo-earthquake events are recognized along the Milun Fault during the late Holocene, including the 2018 and 1951 historical earthquakes and three prehistoric events constrained by calibrated radiocarbon ages (Table 3). Because event ages are expressed as probability ranges rather than single calendar dates, recurrence intervals are evaluated as permissible time windows bounded by the youngest and oldest limits of successive events.

The interval between the 2018 and 1951 earthquakes is precisely known (67 years). The interval between the 1951 event and Event 3 ranges from ≈353–784 years, whereas the interval between

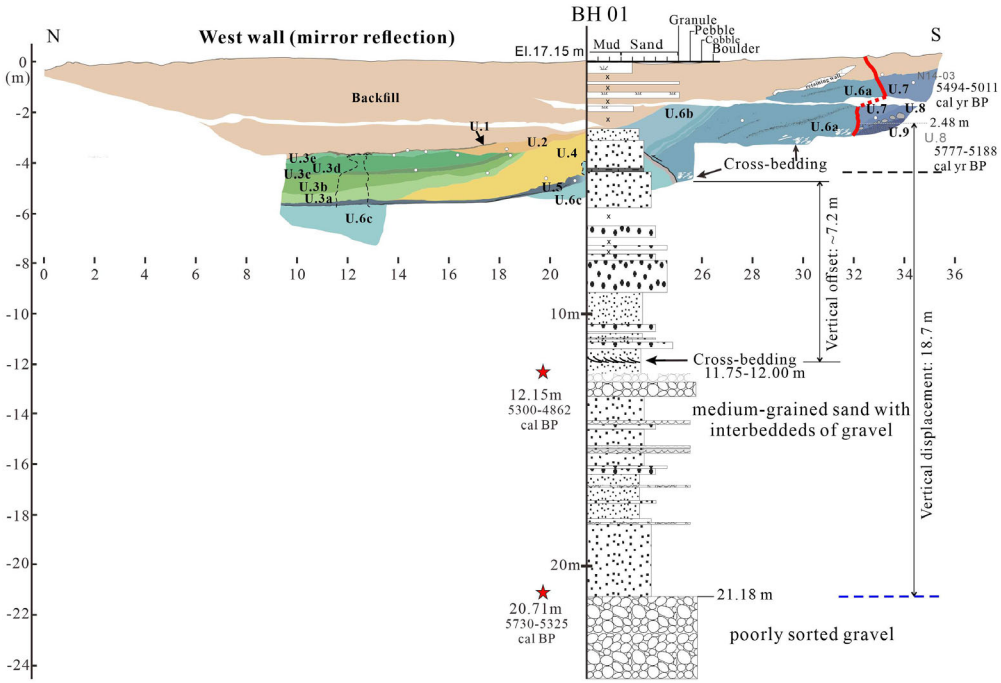

FIGURE 9 | Correlation of boreholes BH01 and Trench 1.

TABLE 3 | Paleo-earthquake events derived from the trenches.

Even	Evidence	Occurrence Time	Interval (yr)	Total slip (m)
1	Surface rupture	2018.02.06		undeterminable
			67	
2	Colluvial Wedge	1951.10.22		undeterminable
			353-784	
3	Folded growth strata	783-352 yr BP		1.12-1.23
			519-2009	
4	Liquefaction	2361-1302 yr BP		0.98-1.0
			0-188	
5	Colluvial Wedge	3185-2303 yr BP		0.51-0.6

Events 3 and 4 ranges from ≈519–2009 years. Even when only minimum permissible separations are considered, inter-event times differ by more than a factor of five, indicating substantial variability in recurrence spacing.

Although calibrated age ranges introduce chronological uncertainty, the magnitude of the variability exceeds what can reasonably be attributed to dating error alone. In particular, the contrast between the short historical interval (67 years) and the minimum prehistoric interval (>350 years) remains evident regardless of overlap in calibrated age ranges. The partial overlap between Events 4 and 5 reflects the limited resolution of radiocarbon dating; however, stratigraphic superposition independently establishes their sequential order. While precise inter-event durations for older events cannot be uniquely defined, the available evidence does not support strictly periodic recurrence.

The observed variability is consistent with the structurally distributed architecture of the Milun Fault zone. Trench exposures reveal a steep principal fault accompanied by several subsidiary branch faults, indicating that slip near the surface is not always localized on a single discrete plane. Rupture during successive earthquakes may therefore involve different combinations of the principal and branch faults, producing spatially variable surface deformation and uneven preservation of stratigraphic evidence at a single trench site. The limited measurable vertical displacement in the trench associated with the 2018 earthquake further demonstrates that not all earthquakes generate equivalent stratigraphic signatures.

Accordingly, the variability in recurrence intervals inferred for the Milun Fault is interpreted to reflect, at least in part, limitations in the preservation and detection of paleo-earthquake evidence, rather than solely true variability in earthquake recurrence. While deformation in transpressional plate-boundary settings may involve complex fault systems at depth, the trench-scale observations primarily constrain how individual events are recorded near the surface. These limitations should be considered when interpreting recurrence patterns from paleoseismic data.

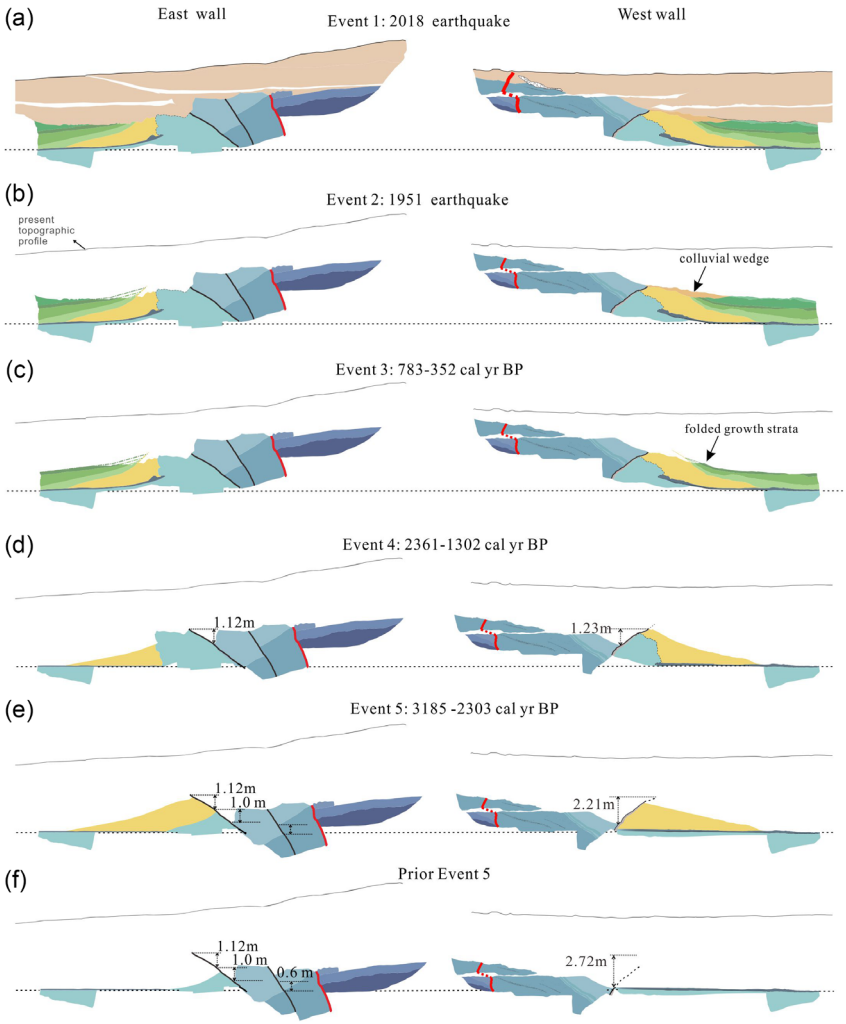

FIGURE 10 | Sequential restoration of Trench 1 showing the progressive reconstruction of fault displacement associated with individual paleoearthquake events. Each panel represents the interpreted stratigraphic configuration following restoration of cumulative displacement for a specific event. (a) Event 1: 2018 Earthquake. (b) Event 2: 1951 earthquake. (c) Event 3: 783-352 cal yr BP. (d) Event 4: 2361-1302 cal yr BP. (e) Event 5: 3185-2303 cal yr BP. (f) Prior Event 5. Detailed explanations of each restoration stage are provided in the text.

5.4 | Structural Context and Implications for Rupture Expression and Paleoseismic Preservation

The Milun Tableland occupies the northernmost onshore segment of the Longitudinal Valley plate-boundary suture between the Eurasian and Philippine Sea plates, within a tectonically complex transition from collision to subduction. Previous studies have proposed contrasting structural interpretations based on geological, geodetic, and geophysical observations (Lin and Hsiao 1998; Shyu et al. 2016; Yen et al. 2019; Lin et al. 2021). Lin and Hsiao (1998) interpreted the tableland as a compressional strike-slip wedge formed through strain partitioning among multiple left-lateral faults, producing a positive flower-structure geometry. In contrast, Shyu et al. (2016) suggested that uplift may be related to a deeper south-dipping reverse fault system rooted in a regional detachment at ~10 km depth. Lin et al. (2021) further proposed that the Milun Tableland represents the onshore expression of a transpressional pop-up structure extending offshore into the southern Hualien Ridge.

Stratigraphic relationships documented in this study indicate that the Milun Tableland emerged above sea level at ≈3.2 ka, providing an independent temporal constraint on surface uplift. Coseismic deformation during the 2018 Mw 6.4 Hualien earthquake produced heterogeneous uplift of up to ~45 cm, accompanied by clockwise rotation and southward tilting, as revealed by InSAR and GPS-derived 3D displacement fields (Yen et al. 2019). These observations indicate that deformation of the Milun Tableland is not confined to a single discrete structure but is distributed across a broader structural domain.

New trench and borehole observations further constrain the shallow geometry of the Milun Fault. Trench 1 exposes a steeply east-dipping principal fault (dip ~ 80°) accompanied by several subsidiary branch faults with shallower dips. Borehole correlations indicate that the principal fault maintains a steep geometry to depths of at least ~20 m (Figure 11). In contrast, Trench 2 reveals minor normal faults with vertical separations of up to ~15 cm. These structures, together with reverse-oriented

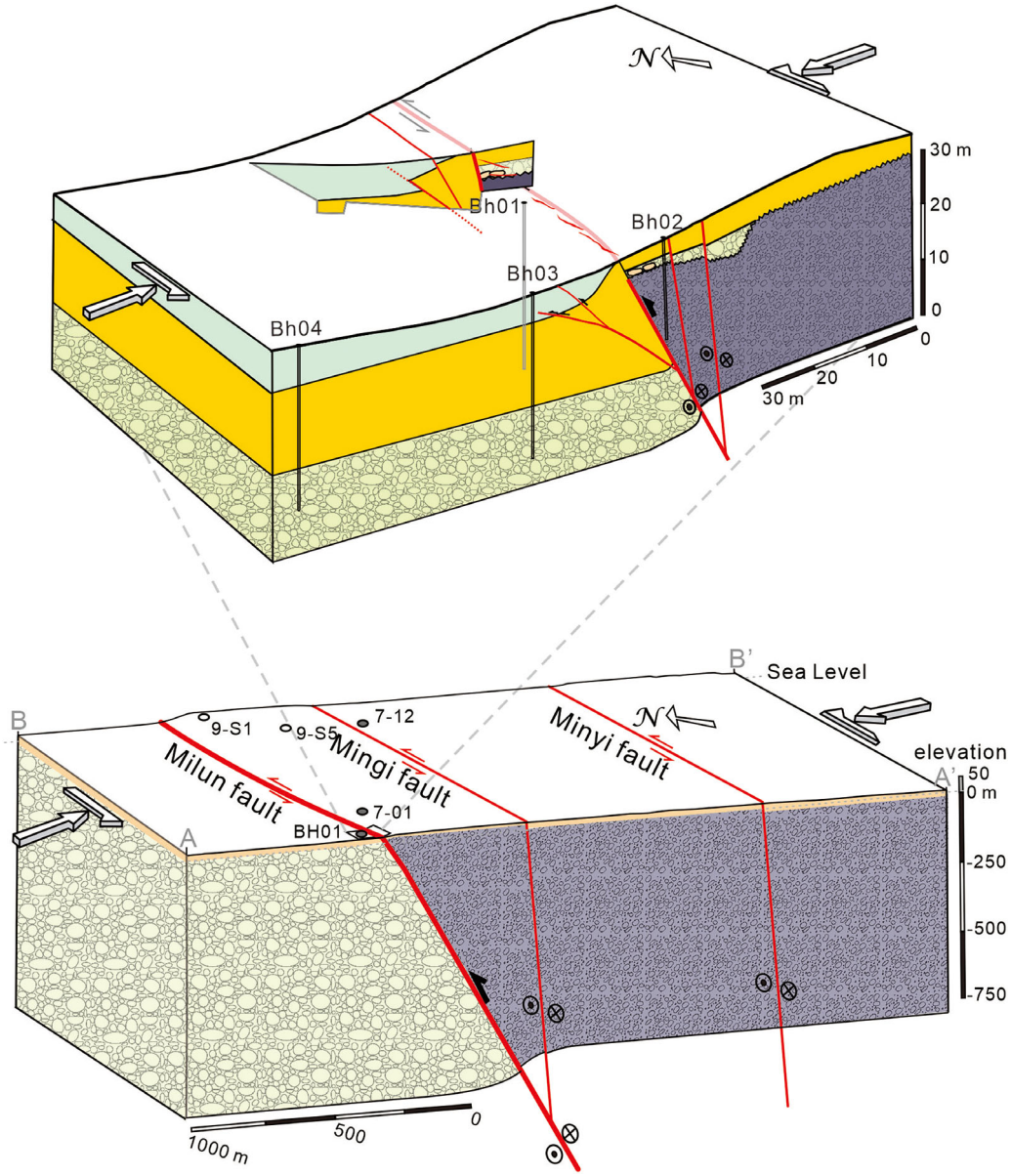

FIGURE 11 | Conceptual block diagrams illustrating the near-surface and deeper structural architecture of the Milun Fault in a transpressional setting. The upper diagram shows the steeply east-dipping main fault and associated subsidiary branches at shallow depth. The lower diagram presents a schematic cross section illustrating distributed deformation beneath the Milun Tableland.

subsidiary faults, are interpreted as manifestations of heterogeneous deformation associated with forced folding above a deeper reverse basement fault system (Ameen 1990), in which the Milunpi Conglomerate acts as a relatively rigid structural basement. At greater depth, Ma et al. (2024) identified the Milun Fault as a steep, east-dipping structure (~70°) intersected by the MiDAS borehole at depths of ~490–520 m, supporting a through-going, high-angle geometry.

These results demonstrate that near the surface, the Milun Fault is expressed as a principal fault accompanied by subsidiary branch faults within a zone of distributed deformation several tens of meters wide. Such m-scale structural complexity is commonly observed in near-surface fault zones and likely reflects deformation within unconsolidated or weakly consolidated sediments, rather than crustal-scale structural partitioning. Therefore, the trench observations do not imply the presence of multiple seismogenic-scale fault segments comparable to those documented in systems such as the 2010 Darfield earthquake (e.g., Litchfield et al. 2014; Boese et al. 2012). Instead, the significance of the observed near-surface deformation lies in its influence on rupture expression and the preservation of paleoseismic evidence. Slip during individual earthquakes may be distributed among the principal fault and subsidiary structures near the surface, leading to spatially variable deformation and incomplete or discontinuous stratigraphic records at individual trench sites. As a result, the paleoseismic record may not capture all surface-rupturing events or may record them incompletely. The irregular inter-event intervals inferred for the Milun Fault are therefore interpreted as reflecting limitations in event preservation and exposure, rather than direct control by shallow structural complexity. This highlights the importance

of considering near-surface deformation processes when interpreting paleoseismic records in collision–subduction transition zones.

6 | Conclusions

This study integrates trench investigations, borehole constraints, stratigraphic analysis, and geological cross sections to investigate the shallow structure, paleo-seismic history, and deformation behavior of the Milun Fault beneath the Milun Tableland. Trench stratigraphy documents five paleo-earthquake events, including the 2018 and 1951 historical earthquakes, as well as three prehistoric events dated to 783–352 cal yr BP, 2361–1302 cal yr BP, and 3185–2303 cal yr BP. These events indicate repeated surface-rupturing deformation during the late Holocene. Stratigraphic relationships further indicate that the Milun Tableland emerged above sea level at ≈3.2 ka, providing an important temporal constraint on the onset of surface uplift. The occurrence of multiple paleo-earthquakes after emergence suggests that uplift of the Milun Tableland was accomplished through cumulative deformation over several seismic events, rather than a single large earthquake.

Analysis of inter-event times reveals highly variable earthquake recurrence intervals, ranging from less than one hundred years to more than one thousand years. This variability, together with the absence of consistent vertical displacement during the 2018 earthquake, suggests that the Milun Fault does not exhibit characteristic earthquake behavior and likely lacks a fixed recurrence interval. The trench record also implies that some paleo-earthquake events may not be preserved, leading to an underestimation of the total number of earthquakes.

Trench and borehole observations reveal a steeply dipping main fault strand accompanied by multiple subsidiary branch faults, indicating that near-surface deformation is distributed among several fault strands. Combining these observations with deeper structural constraints, we propose a multiscale geological model in which sustained reverse left-lateral motion along the Milun Fault generates fault branching, forced folding, and heterogeneous deformation near the surface.

These results emphasize that paleo-seismic records along complex plate-boundary faults may reflect variable slip behavior and incomplete event preservation. For the Milun Fault, both the emergence history of the Milun Tableland and the irregular recurrence of paleo-earthquakes underscore the importance of integrating trench data with structural and stratigraphic constraints when assessing long-term fault activity and seismic hazard.

Acknowledgments

We thank Dr. Kae-Shyuan Shieh for assistance with nannofossil identification, and Dr. Shing-Lin Wang for guidance on radiocarbon dating. This research was partially supported by the National Science Council in Taiwan through Grant MOST 106-2116-M-008-005.

Funding

This study was supported by the National Science Council in Taiwan (Grant MOST 106-2116-M-008-005).

Data Availability Statement

The data that support the findings of this study are available on request from the corresponding author. The data are not publicly available due to privacy or ethical restrictions.

References

Ameen, M. S. 1990. "Macrofaulting in the Purbeck-Isle of Wight Monocline." *Proceedings of the Geologists' Association* 101, no. 1: 31–46.

Boese, C. M., J. Townend, E. G. Smith, and T. Stern. 2012. "Microseismicity and Stress in the Vicinity of the Alpine Fault, Central Southern Alps." *New Zealand. Journal of Geophysical Research: Solid Earth* 117: B02302.

Bonilla, M. G. 1975. "A Review of Recently Active Faults in Taiwan." *U.S. Geological Survey Open-File Report 75-41, Version 1.1* 42. U.S. Department of the Interior U.S. Geological Survey. http://geopubs.wr.usgs.gov/open-file/of75-41/.

Chemenda, A. I., R. K. Yang, J. F. Stephan, E. A. Konstantinovskaya, and G. M. Ivanov. 2001. "New Results from Physical Modelling of Arccontinent Collision in Taiwan: Evolutionary Model." *Tectonophysics* 333: 159–178.

Chen, C. F. 2013. "Seismotectonic Characteristics of the Northernmost Part of the Longitudinal Valley Suture, Eastern Taiwan." Master's thesis, 112. National Taiwan University.

Chen, W. S. 2004. "Trench Excavation and Paleoseismology Research Project 3/5. Central Geological Survey." *Ministry of Economic Affairs* Final Report.

Chen, W. S., N. T. Yu, and H. J. Yang. 2012. "Investigation Project on the Structural Characteristics of Major Active Faults: Analysis and Evaluation of Active Fault Characteristics 2/4. Central Geological Survey." *Ministry of Economic Affairs* Final Report. no. 101-9: 130.

Cheng, S. N., T. T. Yu, Y. T. Yeh, and C. H. Chang. 1997. "Relocation of the 1951 Hualien–Taitung Earthquake Sequence." in Proceedings of the Symposium on Meteorological Analysis and Forecasting: Commemorating 100 Years of Meteorological Service in Taiwan (Oceanography and Seismology Volume), 660–669. Geological Society of China in cooperation with the institute of Earth Sciences, Academia Sinica.

Chi, W. R., H. M. Huang, and J. C. Wu. 1983. "Ages of the Milun and Pinanshan Conglomerates and Their Bearings on the Quaternary Movement of Eastern Taiwan." *Proceeding of the Geological Society of China* 26: 67–75.

Heaton, T. J., P. Köhler, M. Butzin, et al. 2020. "Marine20-the Marine Radiocarbon Age Calibration Curve (0-55,000 Cal BP)." *Radiocarbon* 62, no. 4: 779–820. https://doi.org/10.1017/RDC.2020.68.

Hsieh, M. L., and L. S. Teng. 1994. "The Facies and Sedimentary Environment of the Milun Conglomerate." *Ti-Chih (geology in Chinese)* 14, no. 1: 201–217.

Hsu, T. L. 1956. "Geology of the Coastal Range, Eastern Taiwan." *Bulletin Geological Survey of Taiwan* 8: 15–63.

Hsu, Y. C., W. S. Chen, J. C. Lee, et al. 2019. "Investigating the Structure of the Milun Fault from Surface Ruptures of the 2018 Hualien Earthquake. Terrestrial." *Atmospheric and Oceanic Sciences* 30, no. 5: 557–572.

Huang, S. Y., J. Y. Yen, B. L. Wu, I. C. Yen, and R. Y. Chuang. 2019. "Investigating the Milun Fault: The Coseismic Surface Rupture

Zone of the 2018/02/06 ML. 6.2 Hualien Earthquake, Taiwan." *Terrestrial, Atmospheric, Oceanic Sciences* 30, no. 3: 311–335.

Konishi, K., A. Omuro, and K. Tashio. 1968. "234U-230Th Dating of Some Late Quaternary Coralline Limestone from Southern Taiwan (Formosa)." *Geology and Palaeontology of Southeast Asia* 5: 211–224.

Kuo, Y. T., Y. Wang, J. Hollingsworth, et al. 2019. "Shallow Fault Rupture of the Milun Fault in the 2018 Mw 6.4 Hualien Earthquake: A High-Resolution Approach from Optical Correlation of Pleiades Satellite Imagery." *Seismological Research Letters* 90, no. 1: 97–107.

Lee, S. J., T. C. Lin, T. Y. Liu, and T. P. Wong. 2019. "Fault-to-Fault Jumping Rupture of the 2018 Mw 6.4 Hualien Earthquake in Eastern Taiwan." *Seismological Research Letters* 90, no. 1: 30–39.

Lin, C. C. 1969. "Holocene Geology of Taiwan." *Acta Geologica Taiwanica* 13: 83–126.

Lin, C. W., W. S. Chen, Y. C. Liu, and P. T. Chen. 2009. "Milun Fault." *Special Publication of the Central Geological Survey* 23: 11–20.

Lin, L. K., S. K. Hsu, C. H. Tsai, et al. 2021. "Hualien Ridge: A Tectonic Ridge Transitioning from Plate Collision to Subduction." *Tectonophysics* 816: 229010.

Lin, M. S., and C. L. Hsiao. 1998. "Strike-Slip Tectonics in the Milun Conglomerate Terrace." *Journal of the Eastern Taiwan Studies* 3: 13–29.

Litchfield, N. J., R. Van Dissen, R. Sutherland, et al. 2014. "A Model of Active Faulting in New Zealand." *New Zealand Journal of Geology and Geophysics* 57, no. 1: 32–56.

Ma, K. F., S. Specht, L. W. Kuo, et al. 2024. "Broad-Band Strain Amplification in an Asymmetric Fault Zone Observed from Borehole Optical Fiber and Core." *Communications Earth & Environment* 5, no. 402: 1–13.

Rau, R. J., K. H. Chen, and K. E. Ching. 2007. "Repeating Earthquakes and Seismic Potential along the Northern Longitudinal Valley Fault of Eastern Taiwan." *Geophysical Research Letter* 34: L24301.

Reimer P. J., W. Austin, E. Bard et al. 2020. "The IntCal20 Northern Hemisphere Radiocarbon Age Calibration Curve (0-55 Cal kBP." *Radiocarbon* 62: 4, 725–757.

Reimer, P. J., T. A. Brown, and R. W. Reimer. 2004. "Discussion: Reporting and Calibration of Post-Bomb 14C Data." *Radiocarbon* 46, no. 3: 1299–1304.

Reimer, R. W., and P. J. Reimer. 2026. "CALIBomb [WWW Program]." Accessed February 22, 2026. http://calib.org.

Shih, T. T., J. C. Chang, C. E. Hwang, C. D. Shih, G. S. Yang, and Y. M. Sunlin. 1983. "A Geomorphological Study of Active Faults in Northern and Eastern Taiwan." *Geographical Research NTNU* 9: 20–72.

Shyu, J. B. H., C. F. Chen, and Y. M. Wu. 2016. "Seismotectonic Characteristics of the Northernmost Longitudinal Valley, Eastern Taiwan: Structural Development of a Vanishing Suture." *Tectonophysics* 692: 295–308.

Stuiver, M., and P. J. Reimer. 1993. "Extended 14C Data Base and Revised CALIB 3.0 14C Age Calibration Program." *Radiocarbon* 35, no. 1: 215–230.

Tung, H., H. Y. Chen, Y. J. Hsu, J. C. Hu, Y. H. Chang, and Y. T. Kuo. 2019. "Triggered Slip on Multifaults after the 2018 Mw 6.4 Hualien Earthquake by Continuous GPS and InSAR Measurements. Terrestrial, Atmospheric." *Oceanic Sciences* 30, no. 3: 285–300.

Wang, J. H. 2024. "A Catalogue of Historical and Instrumentally-Recorded Ms ≥ 7 Earthquakes in Taiwan." *Earth and Planetary Science* 3, no. 2: 41–59.

Wang, S. L., Y. Y. Lee, C. C. Shen, et al. 2025. "Marine Reservoir Age Correction (ΔR) for the Taiwan Strait and the Northeastern South China Sea since the Early Mid-Holocene." *Radiocarbon* 67, no. 5: 1117–1134. https://doi.org/10.1017/RDC.2025.10146.

Wu, B. L., J. Y. Yen, S. Y. Huang, Y. T. Kuo, and W. Y. Chang. 2019. "Surface Deformation of 0206 Hualien Earthquake Revealed by the Integrated Network of RTK GPS. Terrestrial." *Atmospheric and Oceanic Sciences* 30, no. 3: 301–310.

Wu, Y. M., H. Mittal, T. C. Huang, B. M. Yang, J. C. Jan, and S. K. Chen. 2019. "Performance of a Low-Cost Earthquake Early Warning System (P-Alert) and Shake Map Production during the 2018 Mw 6.4 Hualien, Taiwan, Earthquake." *Seismological Research Letters* 90, no. 1: 19–29.

Yamaguchi, M., and Y. Ota. 2002. "Tectonic and Paleoseismological Significance of Holocene Marine Terraces on the East Coast of Coastal Range." *Taiwan. Journal of Geography (in Japanese)* 111, no. 3: 323–340.

Yang, G. S. 1986. *The Geomorphological Study of Active Faults in Taiwan: Special Discussion on the Relationship between Active Faults and Geomorphic Surfaces [dissertation]* Chinese Culture University.

Yang, Y. C. 1953. "The Hualien Earthquake of 1951." *Hualien Wenxian (Hualien Historical Journal), inaugural issue* 1: 67–71.

Yen, J. Y., C. H. Lu, R. J. Dorsey, et al. 2019. "Insights into Seismogenic Deformation during the 2018 Hualien, Taiwan, Earthquake: Sequence from InSAR, GPS, and Modeling." *Seismological Research Letters* 90, no. 1: 78–87.

Yu, S. B., H. Y. Chen, and L. C. Kuo. 1997. "Velocity of GPS Stations in the Taiwan Area." *Tectonophysics* 274: 41–59.

Supporting Information

Additional supporting information can be found online in the Supporting Information section. **Figure S1**: South wall of the 2018 trench 2. (a) Orthophoto mosaic of the east wall corresponding to panel (b). (b) Interpreted log of the south wall). Faults and backfill are indicated. **Figure S2**: South wall of the 2018 trench 2. (a) Orthophoto mosaic of the east wall corresponding to panel (b). (b) Interpreted log of the south wall). Faults and backfill are indicated. **Figure S3**: Sample locations in Tench 2 and their dating results.